Supplementary Information Appendix for

Rapid enhancement of chemical weathering recorded by extremely light seawater lithium isotopes at the Permian-Triassic boundary

He Sun[a,b], Yilin Xiao[a*], Yongjun Gao[c*], Guijie Zhang[a], John.F. Casey[c], Yanan Shen[a*]

[a]CAS Key Laboratory of Crust-Mantle Materials and Environments, School of Earth and Space Sciences, University of Science and Technology of China, Hefei, 230026, China; [b]Hefei University of Technology, School of Resources and Environmental Engineering, Hefei, 230009, China; and [c]Department of Earth and Atmospheric Sciences, University of Houston, TX 77204-5007, USA.

*Email: ylxiao@ustc.edu.cn, yongjungao@uh.edu, yashen@ustc.edu.cn

Sections:

I. SI Text

- Results
- Lithium isotope as a silicate weathering proxy
- Seawater Li isotope reconstruction
- Models

II. SI Figures (S1-S19)

III. SI Tables (S1-S3)

IV. SI References

I. SI Text

Results

The Li isotope measurements and element data of the Meishan section are shown in Tables S1 and S2. For trace element concentrations, we use the more commonly used term parts per million (ppm) to replace the unit of μg/g (1 ppm=1 μg/g).

Lithium isotope as a silicate weathering proxy

Lithium is a water-soluble trace element, with ^{6}Li enriched in secondary clay minerals formed during chemical weathering of silicate rocks, whereas ^{7}Li partitions preferentially into the associated water (1, 2). Thus, chemical weathering of silicate rocks tends to drive modern-day riverine Li (isotope values that averages $\delta^{7}Li_{Riv} \approx +23‰$ and ranges from +1.2 to +42‰) to be much heavier than its source rocks (upper continental crust an averages $\delta^{7}Li_{Ucc} \approx +1.7‰$) (3-5). However, lithium isotopes are not fractionated during primary silicate minerals dissolution (6). The riverine Li hence consists of two major inputs, one is dissolved load from silicate minerals dissolution (with low $\delta^{7}Li$ and high [Li]) and the other related to secondary clay formation (with high $\delta^{7}Li$ and low [Li]) (2, 3, 7). Congruent weathering, with little or no secondary clay formation, will result in dissolved Li isotope compositions similar to their source silicate bedrocks. On the other hand, incongruent weathering, with abundant secondary clays formation, will lead to heavy dissolved Li isotope signature relative to their source silicate bedrocks (2, 8, 9). Thus, the large Li isotopic variations observed in modern rivers (+1.2 to +42‰) is a function of chemical weathering intensity, which allows Li isotope ratios to be tracers of the extent of silicate weathering (9-11). Moreover, Li is almost solely hosted in silicate minerals, hence riverine Li signals can provide unique information about carbon dioxide consumption during weathering (11, 12).

The Li isotopic composition of seawater reflects the balance between Li input (river water from continental weathering, hydrothermal fluxes from mid-ocean ridge spreading centers, and subduction reflux), removal fluxes (the incorporation into low temperature clays in marine sediments and altered oceanic crust) and their respective isotopic compositions (9, 13). Present-day riverine Li flux ($\sim 10\times10^{9}$ moles/year) is close to hydrothermal flux ($\sim 13\times10^{9}$ moles/year). They are the two dominant sources of dissolved Li to seawater (9). HT vent fluid from high temperature

alteration of mid ocean ridge basalt (δ^7Li_{MORB} ~ +4‰) exhibit slightly fractionated but almost uniform δ^7Li values (~ +8‰) (14, 15). Subduction reflux from slab dehydration and breakdown of marine clays has been argued to have an almost constant Li flux (~6×10^9 moles/year) and a fixed isotopic composition of ~ +16‰, and thus would have a minor influence on marine Li isotope change (9). The flux-weighted isotopic composition of input Li (river + HT+ subduction reflux) for modern seawater is ~ +15‰. At steady state, the lithium removal flux should equal to the input flux. The isotopic fractionation during removal Li from seawater by secondary clays formation is a constant value ($\Delta_{SW\text{-}SED} = \delta^7Li_{SW}\text{-}\delta^7Li_{Sink} \approx 16‰$) and drives seawater to be isotopically heavy (modern seawater δ^7Li ~ +31‰) (16-18). Marine carbonate formation, due to its low Li concentrations and small isotopic fractionation factor (~ 3-5‰), does not affect seawater Li significantly (11, 19, 20).

Seawater Li isotope reconstruction

The sediment-related sinks for Li in the ocean exhibit relatively constant isotope fractionation during clay mineral ($\Delta_{SW\text{-}clay}$ ~ 16‰) and carbonate ($\Delta_{SW\text{-}carbonate}$ ~ 3-5‰) precipitation (16-22). Thus, marine sediments can be used to evaluate the Li isotopic compositions of seawater. Post-Archean Australian Shale (PAAS) normalized Rear Earth Element (REE) diagram of carbonate sediments from the Meishan profile show similar patterns to the marine authigenic carbonate (Fig. S1), indicating that the isotopic shifts of the sediments should represent primary seawater signatures with LREE depletion, positive La anomalies, negative Ce anomalies, and positive Y anomalies (23, 24). The δ^7Li and [Li] values of measured sediment samples from the Meishan section show a large range of variation, with lower [Li] and relatively heavy δ^7Li in Beds 22-24 and higher [Li] and relatively light δ^7Li in Beds 25-34, which is consistent with lithostratigraphy (main text Fig.1b) (25). Clays typically have much higher Li (~ 30-70 ppm) and Al_2O_3 (~ 15-40 wt.%) contents compared to carbonate ([Li] < 6 ppm and Al_2O_3 < 2 wt.%) (5, 16, 18, 21, 26-28). Hence the Al_2O_3-[Li] and Al_2O_3-δ^7Li diagrams are used to estimate the carbonate and clay fractions of samples (Figs. S2-S3). The results show that the lower [Li] values in Beds 22-24 and higher [Li] values in Beds 26-30 are both strongly correlated with Al_2O_3, although with clearly different Al_2O_3/[Li] ratios. Bed 25, however, is deviated from the correlation lines because of high Kaolinite content. Samples from Beds 26-30 are clearly on the mixing line of clays and carbonates, with Al_2O_3/[Li]~0.38. Previous

studies indicate that clays from Beds 26-30 are mainly composed of illite + montmorillonite with ~ 5% Kaolin, while Bed 25 has higher Kaolin content (~ 18%) (29). Because Kaolin have much higher Al_2O_3 contents (up to 45 wt.%) than illite-montmorillonite (~ 15-30 wt.%), samples from Bed 25 show an upward shift to high Al_2O_3 (30-32). The well-defined mixing line (Beds 26-30) intersects with the carbonate trend, constrained as a mixing line of limestone (carbonate + chert) end-members ([Li] ~ 12 ppm, Al_2O_3 ~ 1.8 wt.%). The other end-member composition of clays, however, is difficult to 'precisely' quantify using the Al_2O_3-[Li] diagram. Linear Al_2O_3-[Li] correlation of samples from bed 22-24 display distinct lower slope (Al_2O_3/[Li] ~ 0.17) than mixing line with clays (Al_2O_3/[Li] ~ 0.38). Thus, despite good correlation of Al_2O_3 and [Li], it is unlikely that clays participated in samples from Beds 22-24. Chert, with Al_2O_3/[Li] ~ 0.15 and [Li] ~ 20 ppm, is a more feasible mixing end member with carbonate samples in beds 22-24 (21, 27, 33-36). The mixing of chert is also supported by [Li]-Fe_2O_3, [Li]-B and Sr-Pb diagrams (Figs. S4-S6) (27, 28, 33, 37). These arguments strongly support the contention that chert, rather than clays, is responsible for the observed [Li]-Al_2O_3 correlation in carbonates from Beds 22-24. Unfortunately, the Li isotopic fractionation factor of chert is poorly constrained. Thus, δ^7Li-1/[Li], δ^7Li-CaO, and CaO-1/[Li] diagrams are made to verify the isotopic effect on clays and chert mixing (Figs. S7-S10).

The remarkable correlations of δ^7Li with 1/[Li] and CaO in mudstone samples from Beds 26-34 (Figs. S7-S9), and the relative constant Li isotopic compositions of the claystone from Beds 26-34 (δ^7Li=-0.1 to -0.3‰), argue for the two end-members of mixing (clays and carbonates) both have a relatively steady composition, which indicate that the seawater Li isotopic composition should remain stable during the time interval (~ 0.4 Ma). We use the measured Li isotopic compositions of claystone to represent the Li isotopic compositions of clay end-member, and use the 1/[Li]-CaO, 1/[Li]-δ^7Li, and CaO-δ^7Li diagrams to calculate the [Li], CaO and Li isotopic compositions of the two end-members, with input parameters of $[Li]_{limestone}$ =12 ppm (independently derived from [Li]-Al_2O_3 diagram) and δ^7Li_{clay} = -0.2‰ (measured Li isotopic compositions of claystone from Beds 26-34). Calculation based on mixing model gives [Li] = 45-50 ppm, CaO ~ 0 wt.% and δ^7Li = -0.2‰ for clays, and [Li] = 12 ppm, CaO = 35.5wt.% and δ^7Li = +11.5‰ for limestones. Thus, seawater Li isotope estimations from carbonates (~ +14.5-+16.5‰ at fractionation factor of ~ 3-5‰) and clays (~ +15.8‰ at fractionation factor of ~ 16‰) are in good agreement. Samples from Beds 22-24, however, show variation in δ^7Li independent to Al_2O_3 and 1/[Li]. The poorly linear correlation

in Figure S10 demonstrates that, if [Li] increase from 1.5 ppm to ~ 20 ppm as a result of chert mixing, the δ^7Li only changed ~ 0.6‰. This indicates that, although the fractionation factor is unclear, chert should have Li isotope composition similar to carbonate in the present study. Thus, without the mixing of clays, the carbonate samples (Beds 22-24) could represent primary seawater signatures by adding 3-5‰ fractionation (9, 11, 19, 20, 38). Bed 25, with high Al_2O_3, B and low Ti, Na, Fe, Co concentrations, reflecting its higher Kaolin proportion in clays (Figs. S2-S6) (30, 32). The high Al_2O_3, [Li] (29-39 ppm) and B (up to 117 ppm) concentrations and low δ^7Li values (-0.3~1.0‰) imply clays dominate the Li signal in Bed 25. Therefore, the δ^7Li values of clays in Bed 25 should be similar or slightly lower than whole rock samples, which gives estimated seawater δ^7Li of ~ +16.0‰, similar to Beds 26-30. The calculated seawater Li isotope records and detailed calculation procedures are listed in Table S1.

Models

The steady state box model of the Li cycle in marine system was first established by Misra and Froelich (2012). Here, similar static and dynamic box models were used to explore seawater Li isotope variations. Essentially, seawater Li budget is controlled by its input (river water, hydrothermal fluid, subduction refluxed) and output (clay formation during seafloor alteration and sediment diagenesis) fluxes (2, 9, 11, 15, 17, 39-44). Therefore, the mass balance of Li in seawater gives:

$$\frac{dN}{dt} = F_{input} - F_{output} = F_{Riv} + F_{HT} + F_{SR} - F_{SC} \qquad \text{(Eqn.S1)}$$

where N is the seawater Li reservoir. We use a total Li ~ 3.4×10^{16} moles (inventory of Li in present-day seawater, calculated using a total volume of the oceans ~ 1.33×10^9 km^3 and [Li] ~ 26μM) as a start parameter (9). F_x represents the input and output fluxes (Riv=river, HT=hydrothermal fluid, SR=subduction reflux, SC=Li sink into clays), with start parameters equal to modern Li fluxes (Table S3). The Li isotopic balance in seawater can be presented by equation:

$$\frac{d\delta_{SW}}{dt} = \frac{1}{N}\{F_{Riv}(\delta_{Riv} - \delta_{SW}) + F_{HT}(\delta_{HT} - \delta_{SW}) + F_{SR}(\delta_{SR} - \delta_{SW}) - F_{SC}(\delta_{SC} - \delta_{SW})\} \qquad \text{(Eqn.S2)}$$

where δ_{SW} is the seawater Li isotope composition and δ_x in the right side of the equation represents the isotope ratio of input and output fluxes. Hence, the seawater Li isotopic change in a small time interval (Δt) can be express as:

$$\Delta_{SW} = \frac{\Delta_t}{N}\{F_{Riv}(\delta_{Riv} - \delta_{SW}) + F_{HT}(\delta_{HT} - \delta_{SW}) + F_{SR}(\delta_{SR} - \delta_{SW}) - F_{SC}(\delta_{SC} - \delta_{SW})\} \quad \text{(Eqn.S3)}$$

where 10Kyr time steps were used in our study.

For the steady state model, the Li input and output flux balance with each other, with $F_{input}=F_{output}$. As suggest by previous studies, the subduction reflux has a minor influence on seawater Li isotope changes (9). This term is thus held constant at ~ 6×10^9 moles/year with isotopic composition of ~ +15‰ (42). Therefore, variations in hydrothermal and/or riverine fluxes are the major forces that perturb seawater Li isotopes. The model results for several different assumptions are shown in Figs. S11-S14.

Figure S11 shows the isotopic response to decreasing riverine Li isotope compositions (due to a change in weathering intensity) with constant F_{Riv} and all other parameters for 5Myr. This result shows that, at steady state, riverine Li decrease from +20‰ (incongruent weathering) to +2‰ (congruent weathering) would only result in ~7‰ Li isotopic decline for seawater. Such a process can drive seawater Li isotope down to a minimum of ~ +24‰. To explain the estimated light seawater δ^7Li at PTB (as low as +10‰), increased riverine Li fluxes (increase in weathering rate) with very low isotope value (+2‰, very high weathering intensity) are modeled (Fig. S12). The results show that, with increased F_{Riv}, seawater δ^7Li decreased and exhibit shorter Li residence time. A fifteen-fold higher riverine flux can drive seawater δ^7Li to ~ +19‰. However, continued increase in F_{Riv} cannot lower seawater δ^7Li any further. Therefore, this is still not sufficient to cause the required seawater Li isotopic compositions.

Seawater isotopic responses to variation in F_{HT} are shown in Figure S13. Because the Li isotope compositions of HT vent fluids are controlled by their source rocks (δ^7Li_{MORB} ~ 4‰) with a constant fractionation factor (~ 4‰), the δ^7Li_{HT} is kept constant at 8‰ in the modeling (14, 15, 18, 43, 45, 46). Increase in HT flux alone can change seawater δ^7Li down to ~ +25‰, also not sufficient to cause the required seawater δ^7Li. Figure S14 shows the effect of a combination of the two processes (change in river and HT flux) with light riverine δ^7Li. Given that, at steady state, the Li sink from the oceans is equal to the input fluxes, a combination of the two processes can only result in seawater δ^7Li decrease to ~ +18‰. Hence, for seawater δ^7Li to decrease to observed values at PTB, a dynamic model is needed.

In the dynamic box model, Li sink into clays is a function of the rate of clay formation, seawater Li

concentration and Li partition coefficient of clays. We assume the rate of clay formation and Li partition coefficient to be constant because the process forming clays seems not changed over time. Thus, the seawater Li output is proportional to Li concentrations in seawater, forming a feedback on Li input:

$$F_{SC}^{t} = kN^{t} = k\left(N^{t_0} + \int_{t_0}^{t} F_{input} - \int_{t_0}^{t} F_{SC}\right) \quad \text{(Eqn.S4)}$$

where k is the partition coefficient between seawater and clays. For a small time interval, $\Delta t = t - t_0$, the above formula can be rewrite as:

$$F_{SC}^{t} = \left\{1 + \frac{\Delta t}{N^{t_0}}\left(F_{input}^{t_0} - F_{SC}^{t_0}\right)\right\} \times F_{SC}^{t_0} \quad \text{(Eqn.S5)}$$

Results of dynamic box model are shown in Figs. S15-S17.

Figure S15 shows the seawater Li isotopic response on F_{HT} changes using the dynamic box model. Changing HT flux from 0.5 to 20×10^{10} moles/year (modern F_{HT} is ~1.3×10^{10} moles/year) (15), the seawater δ^7Li minimum varies from +31 to +15‰. A higher HT flux (>20×10^{10} moles/year) could result in low δ^7Li values to ~ +10‰, consistent with the seawater Li isotope ratios at PTB. However, such a high hydrothermal input at PTB seems unrealistic, since there is little geophysical evidence for very fast spreading rates or large ridge volume at end-Permian when global eustatic sea levels are thought to be low (47). The extremely low sea level at the end-Permian and the existence of supercontinent Pangea (320-185Myr) imply the ridge volume was probably less than today (48, 49). Seawater Sr isotope records show increased $^{87}Sr/^{86}Sr$ at the end-Permian, either reflecting higher riverine Sr input or restrained hydrothermal flux (see Fig. S18) (12, 50-53). Therefore, the hydrothermal flux at the end-Permian should be less than or similar to today. Changing riverine Li and its isotope compositions also can account for the observed seawater δ^7Li values (Fig. S16). Increasing the river flux alone for 5 Myr with modern riverine Li isotope values (+23‰) would result in a first decrease, and then ascending δ^7Li trends for seawater. Decreasing the river δ^7Li, with river flux stayed constant, would result in seawater δ^7Li trends similar to Figure S11. Neither process alone has sufficient effect to perturb seawater δ^7Li to the values observed in the Meishan section. Thus, modeling the observed low δ^7Li requires an enhanced riverine Li flux accompanied with very light isotope ratios (Fig. S17). The results indicate that, if the river δ^7Li set at ~ +4‰, the Li flux would have to increase ~ 15-20× to cause the observed seawater δ^7Li (+10-+16‰). Hence, the modeling suggests a process with enhanced weathering rate, which we suggest is the only realistic

approach for explaining the Li isotope variations in seawater at PTB. As discussed in the main text, the onset of PTB was in coincidence with the largest igneous-province (LIP) formation on the Earth, the Siberian Traps (54). The eruption of Siberian Traps has exposed enormous flood basalts (~7×10^6 km^2) to the Earth's surface. Because the weathering rates of minerals decrease with the Bowen reaction sequence (Fig. S19), basalts, mainly composed of pyroxene + plagioclase + olivine + glass, would be weathered very rapidly and highly congruent (few secondary minerals precipitated due to their freshness and aluminum-deficient nature). This combined with hothouse climate and acid rains, may provide favorable conditions for the enhanced weathering rate (55-60).

II. SI Figures S1-S19:

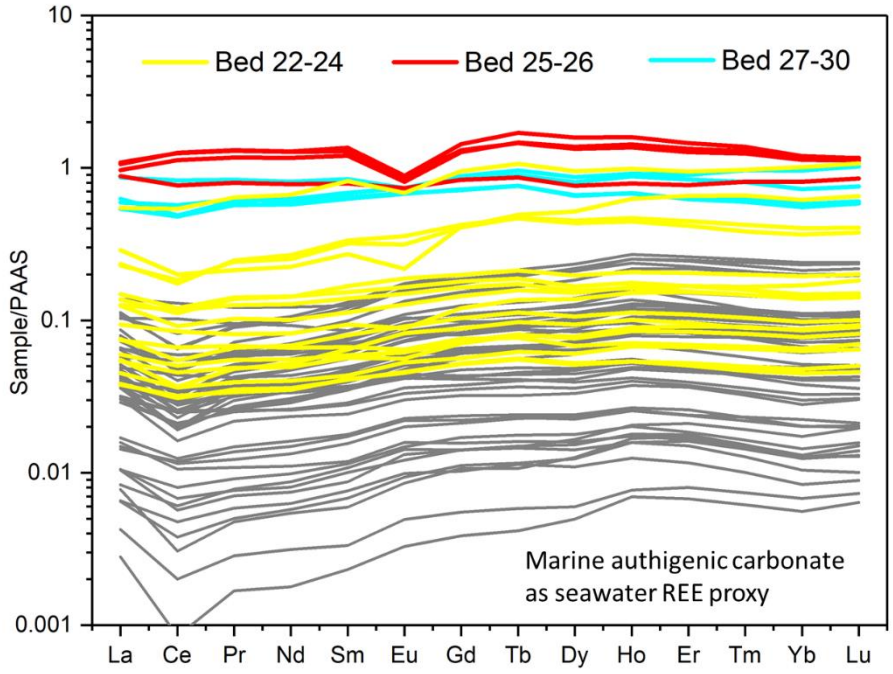

Figure S1. Post-Archean Australian Shale (PAAS) normalized REE patterns of samples from Meishan section and marine authigenic carbonate. The limstones from Beds 22-24 show similar LREE light patterns, positive La anomalies, negative Ce anomalies and low REE concentrations to the marine authigenic carbonate. Claystones from Beds 25-30 show flatter REE patterns but with siginificantly higher REE concentrations than limstones from Beds 22-24, which is a clear signature of marine authigenic clay minerals in more argilaceous beds. PAAS data after ref 23. Marine authigenic carbonate data from ref 24.

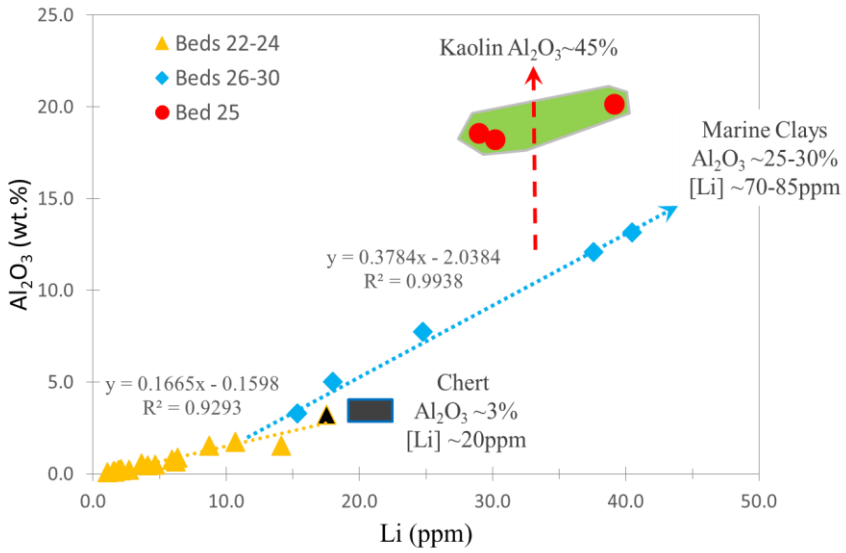

Figure S2. Al_2O_3-[Li] diagram of samples from Beds 22-30, Meishan section. Linear correlations of Beds 22-24 and Beds 26-30 represent mixing lines: mixing of carbonate and chert (yellow line); mixing of carbonate+chert and clays (blue line). Bed 25, due to its higher Kaolin content, is deviated from the mixing line. The well-defined mixing line intersects with the carbonates + chert trend, constrains a limestone (carbonate+ chert) end-member ([Li]~12 ppm, Al_2O_3~1.8wt.%). The average Li and Al concentrations of clays and chert in the Meishan section are consistent with the published values (5, 16, 18, 21, 27, 33-36).

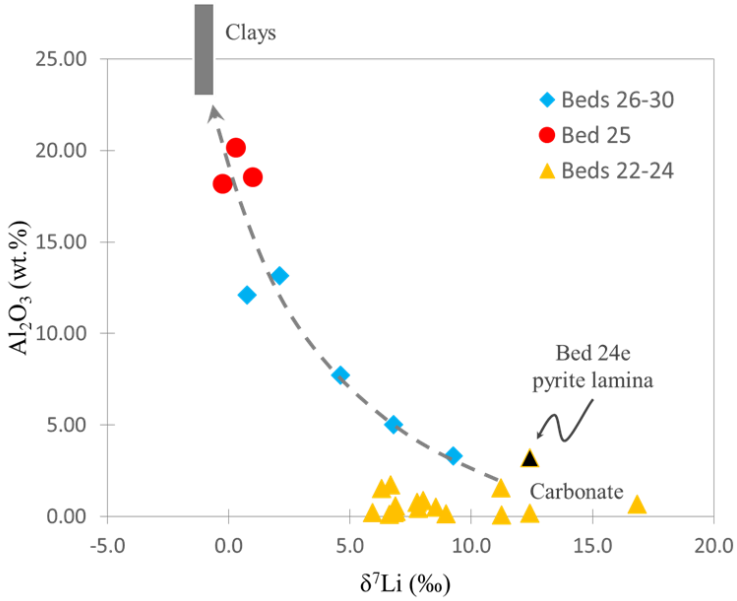

Figure S3. Lithium isotopic ratios and Al_2O_3 variations of samples from Beds 22-30, Meishan section. Beds 25-30 all plot on the mixing trend of carbonates and clays. Beds 22-24, however, show variable δ^7Li independent to Al_2O_3 concentrations and suggest negligible contamination of clays in these samples.

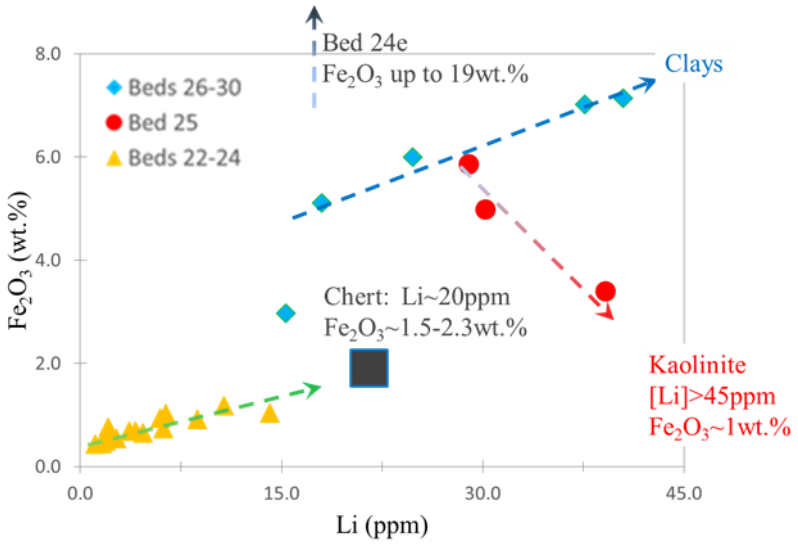

Figure S4. Fe_2O_3 and [Li] variations of Meishan section. Linear correlations of Beds 22-24 (yellow triangle) and Beds 26-30 (blue diamond) represent mixing lines of carbonate with chert and limestone with clays. Bed 24e (red circle), with pyrite lamina, has very high Fe_2O_3 content. Bed 25 has lower Fe concentrations, which could be a signature of Kaolinite (31, 32).

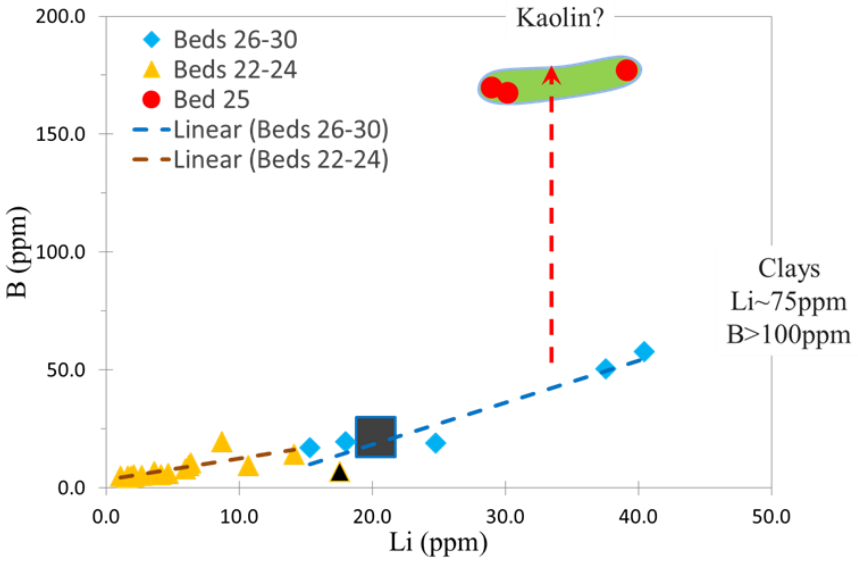

Figure S5. B and Li concentrations of Meishan section. Yellow line (Beds 22-24) and blue line (Beds 26-30) support the mixing trends as suggested by previous figures. Bed 25 has unusually high B concentrations (>150 ppm), probablly indicative of the role of Kaolinite.

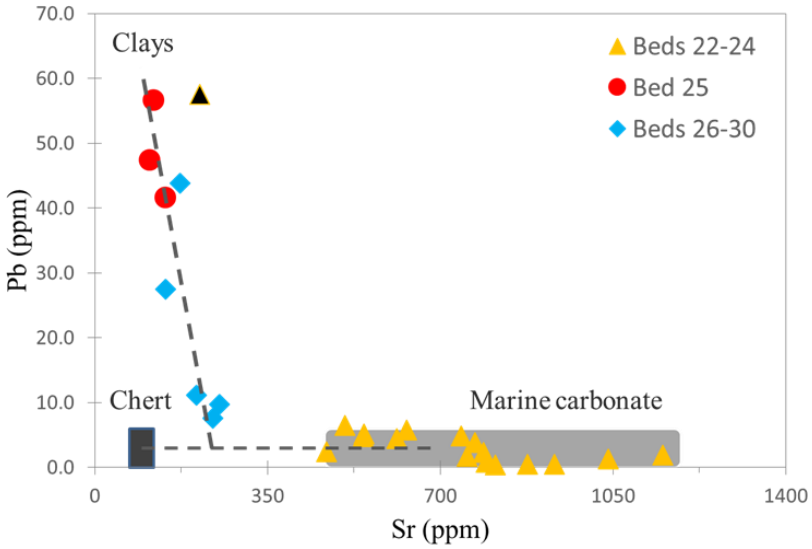

Figure S6. Pb-Sr diagram of Meishan section. Generally, carbonates (grey aera) have high Sr low Pb concentrations, whereas clays have low Sr but high Pb concentrations (27, 28). Chert, with low Sr and Pb concentrations (27, 33), is needed to explain the trends of Beds 22-24 and Beds 25-30. The low Pb concentrations in Beds 22-24 indicate few clays are involved in these samples.

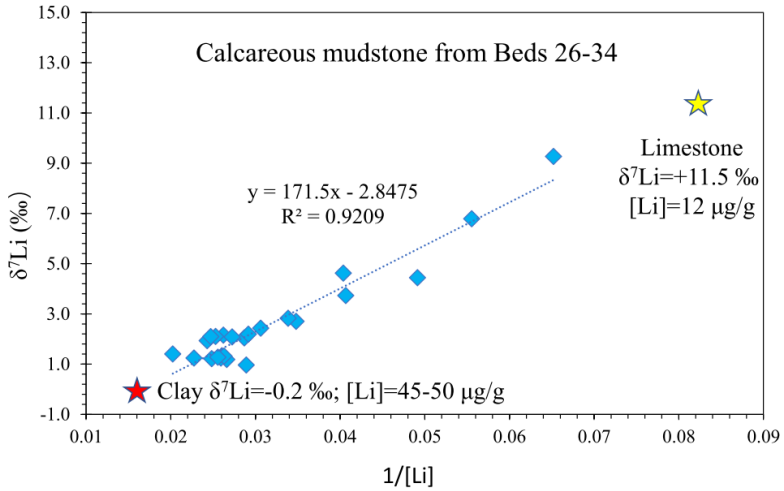

Figure S7. Li concentration (1/[Li]) and isotopic composition of calcarous mudstones from Beds 26-34 of the Meishan section. The well defined mixing line indicates two steady end members: clays and limestones. Using the estimated Li concentrations, the Li isotopic compositions can be calculated, which give δ^7Li ~ -0.2‰ in clays and δ^7Li ~ +11.5‰ in limstones.

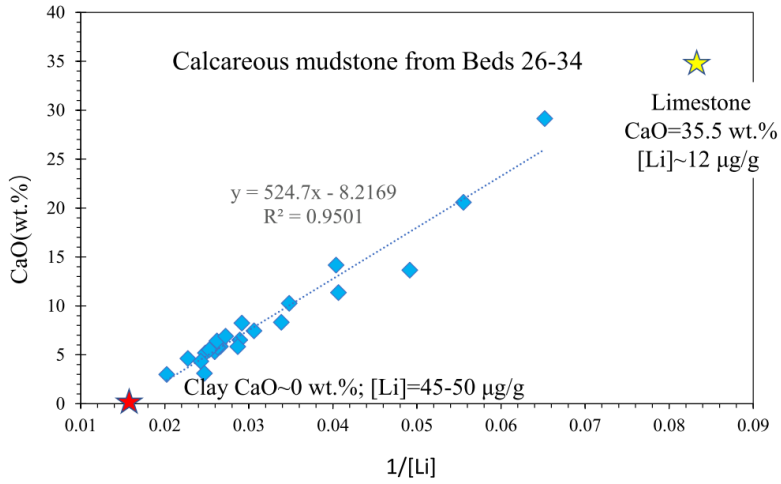

Figure S8. Li concentration (1/[Li]) and CaO contents of calcarous mudstones from Beds 26-34 of the Meishan section. The well defined mixing line gives estimations of the two end members: CaO ~ 0wt.‰ and [Li] = 45-50 ppm in clays and CaO ~ 35.5 wt.‰ and [Li]=12 ppm in limestone.

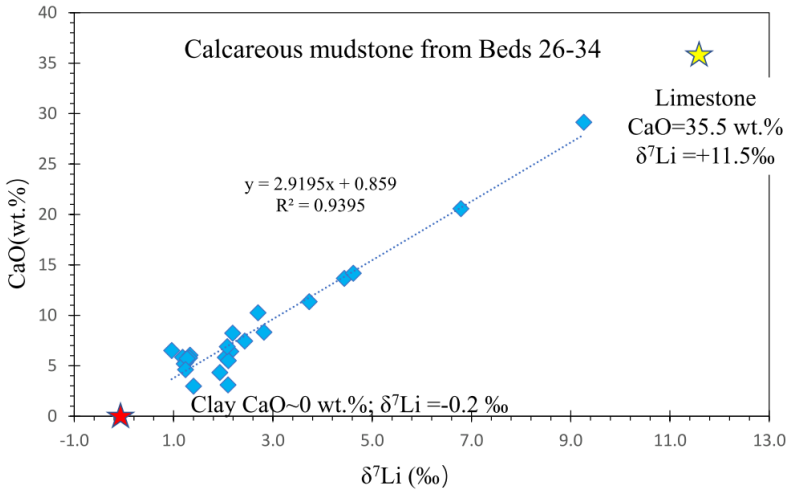

Figure S9. CaO contents vs. δ^7Li diagram for calcarous mudstones from Beds 26-34 of the Meishan section. The corelation trend indicates mixing line of clays and limestones. Estimated end members are: CaO ~ 0wt.%, δ^7Li ~ -0.2‰ in clays and CaO ~ 35.5wt.%, δ^7Li ~ +11.5‰ in limstone.

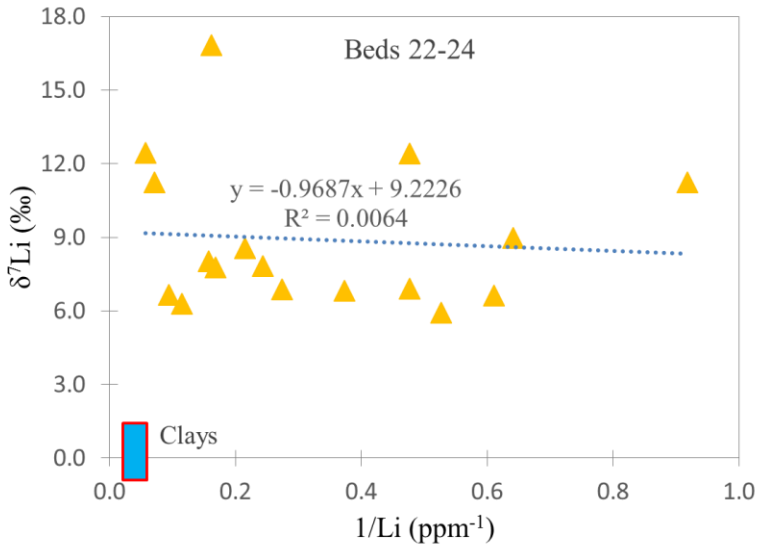

Figure S10. Li concentration and isotopic composition of Beds 22-24 from Meishan section. The poor linear correlation (blue dash line) rules out the contamination of clays. Samples wih low Li concentrations have Li isotope compositions identical with the high [Li] ones. This indicates the chert should have Li isotope composition similar to carbonate in these samples.

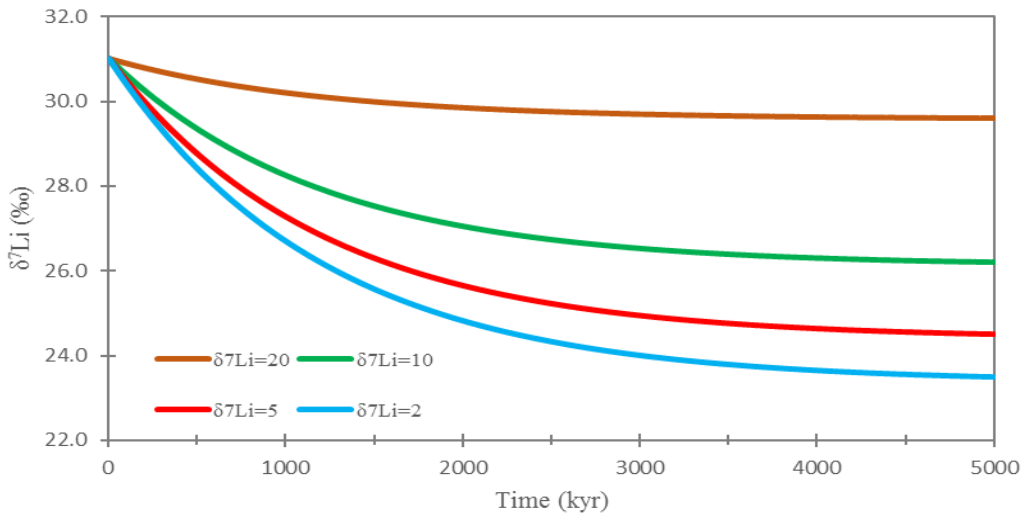

Figure S11. Seawater δ^7Li response to lower riverine Li isotope values of +2, +5, +10, and + 20‰ (based on starting value = current seawater composition of +31‰) over 5Myr . The steady state model is applied.

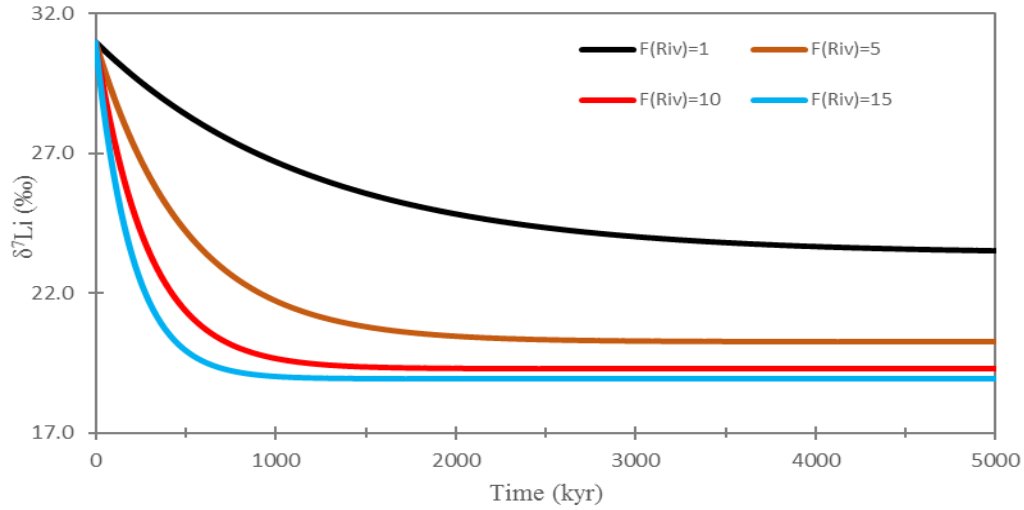

Figure S12. Seawater δ^7Li response to increasing riverine [Li] flux of 1, 5, 10, and 15 times of present-day riverine [Li] flux with a riverine δ^7Li value of +2‰ using a steady state model. Higher fluxes result in shorter times to achieve steady state.

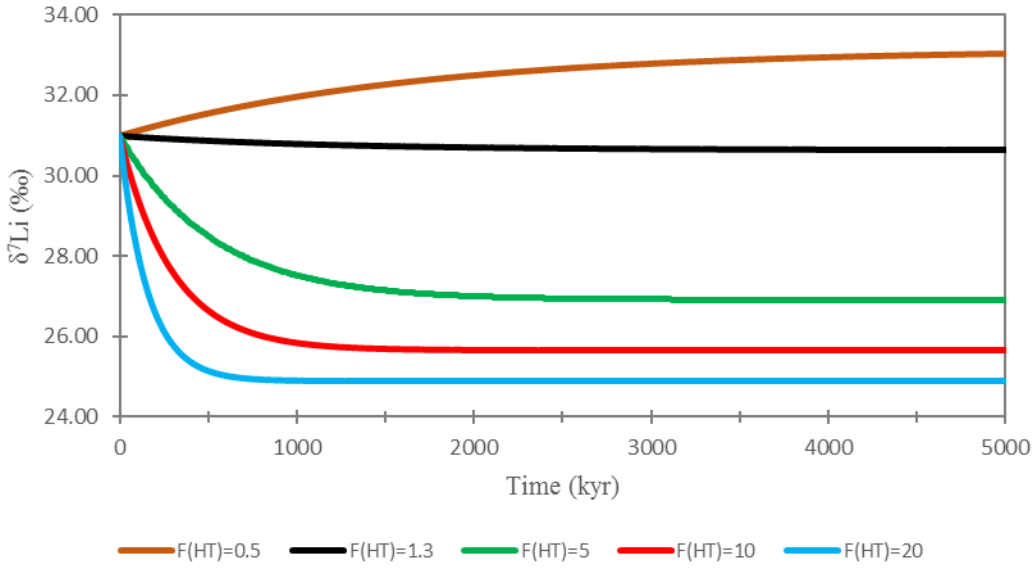

Figure S13. Effect of hydrothermal flux increase (from 0.5× to 20×10^{10}mole/year) for 5Myr, steady state model.

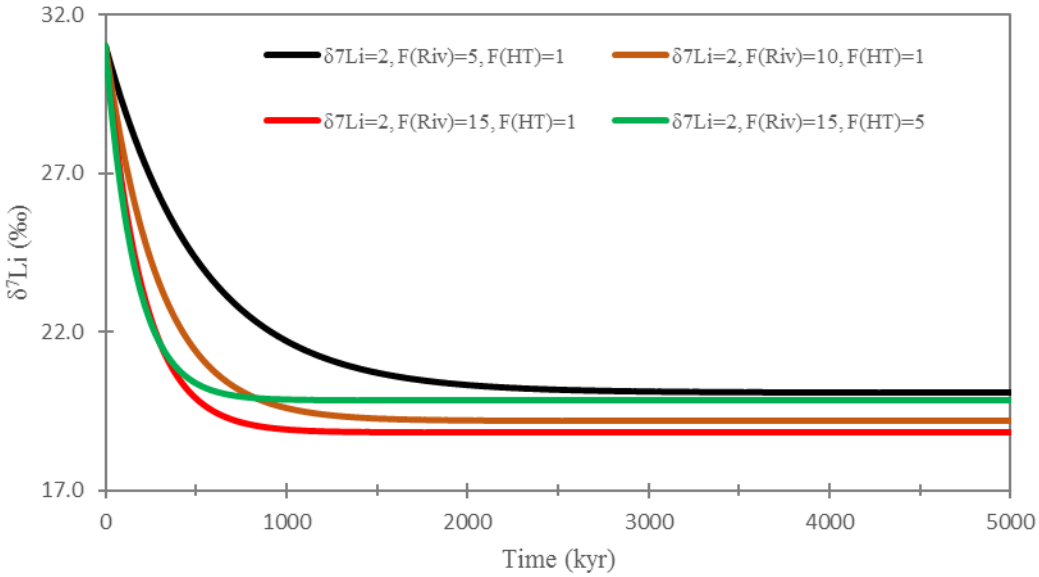

Figure S14. Seawater δ^7Li response to combination of increased riverine flux (with low δ^7Li_{Riv} = +2‰) and hydrothermal flux (with δ^7Li_{HT} = +8‰), steady state model.

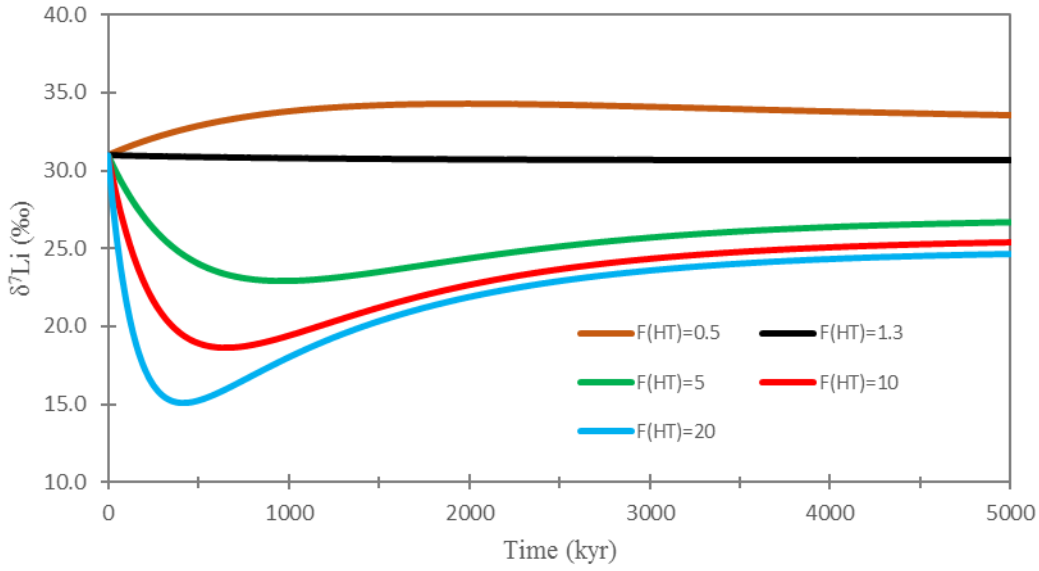

Figure S15. Dynamic model results of increase hydrothermal flux from 0.5× to 20×10^{10}mole/year for 5Myr. Riverine [Li] flux and Li isotopic composition are set to present-day values.

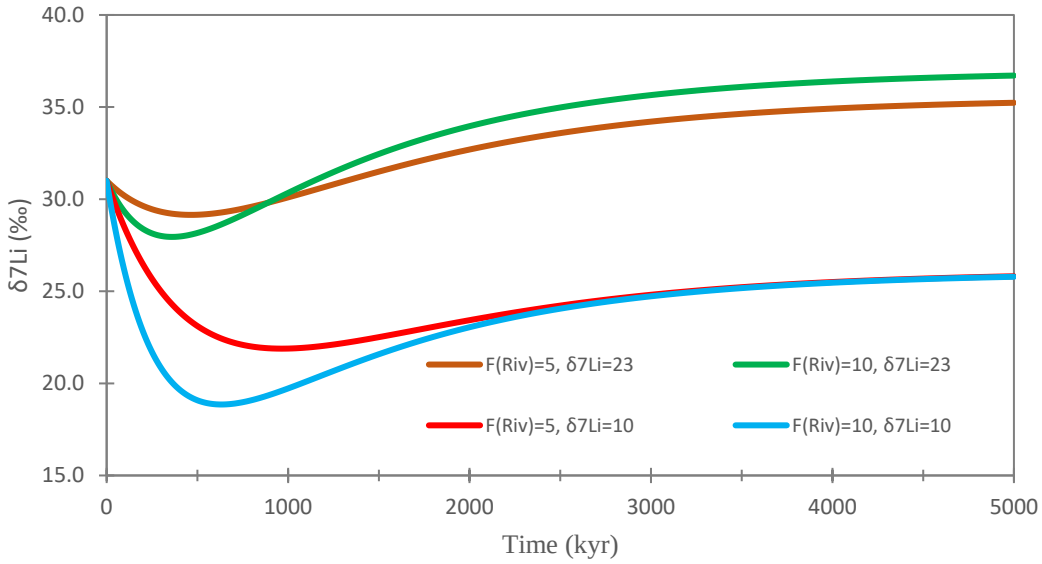

Figure S16. Response of seawater δ^7Li to changes in the riverine flux and isotope ratio, dynamic model.

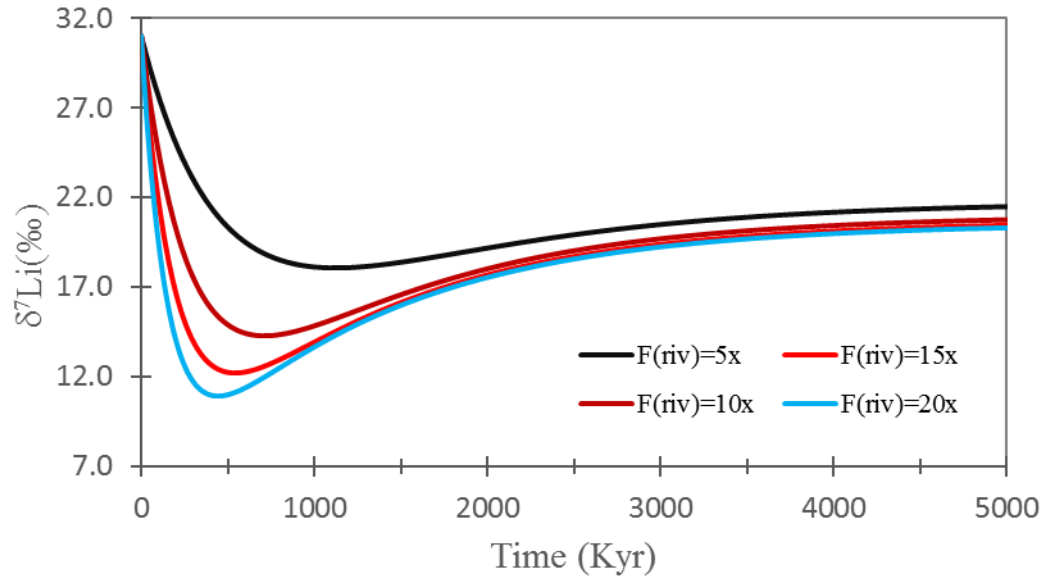

Figure S17. Response of seawater δ^7Li to changes in the riverine flux with a fixed δ^7Li_{Riv} = +4‰, dynamic model. The results indicate the Li flux would have to increase ~ 15-20× to cause the observed seawater δ^7Li (+10-+16‰) at PTB.

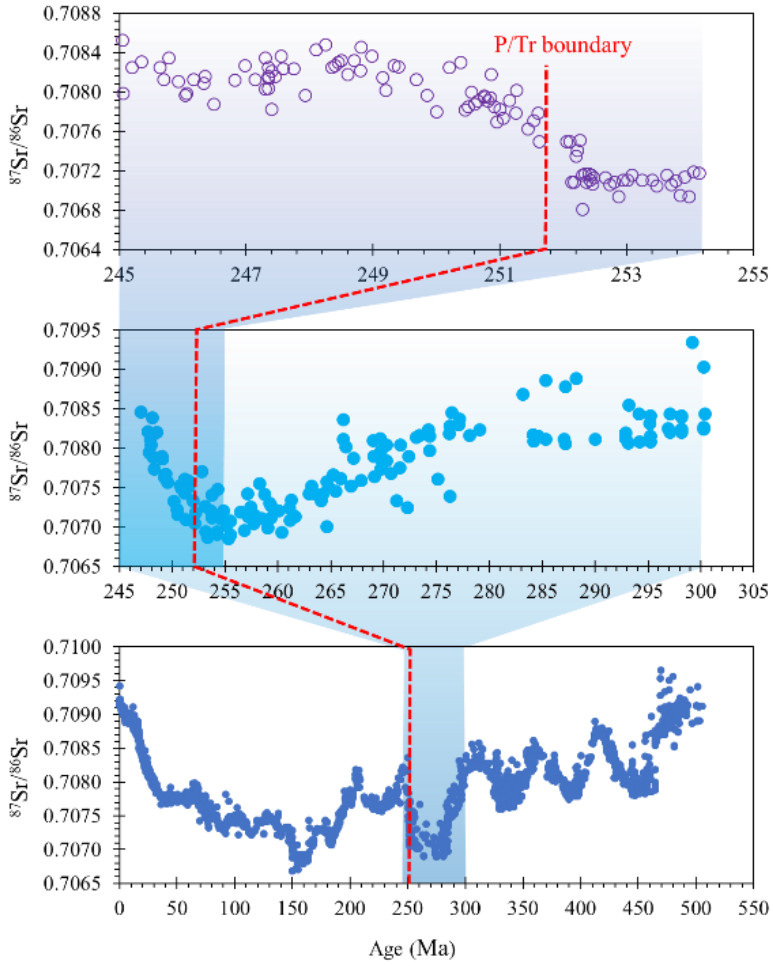

Figure S18. Seawater $^{87}Sr/^{86}Sr$ evolution trend across Permian/Triassic boundary at different time scales, data from Ref (51-53)

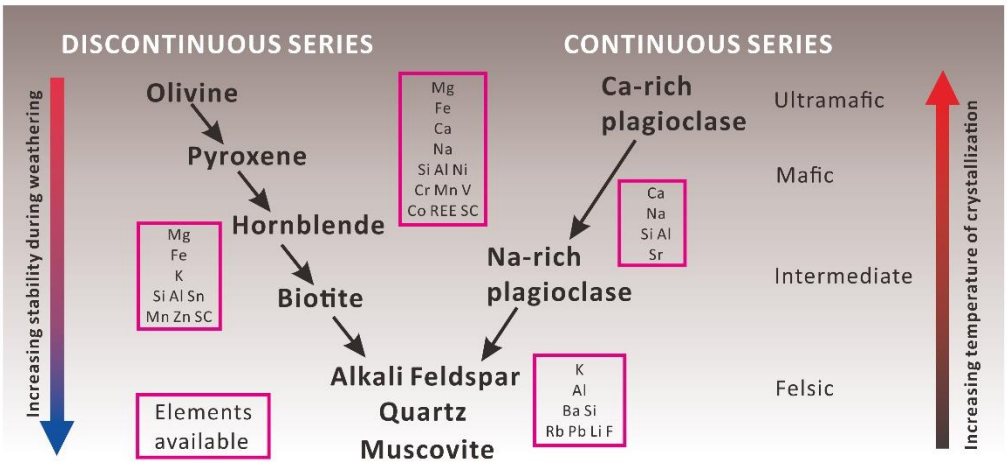

Figure S19. Silicate mineral stability during weathering. Decreasing temperature of crystallization results in increased stability during weathering. Revised after Ref (61).

III. SI Tables (S1-S3)

Table S1. Lithium isotope and [Li] data of the Meishan section, also shown the estimated seawater Li isotope compositions. The analysis precision for Li isotopic compositions are <0.5‰ (2SD). We adopt an estimated error of ~2‰ (±1‰) for the calculated seawater δ^7Li values.

Formation	Sample Name	Rock type	Height	CaO	Li	δ^7Li	δ^7Li_{carb}	Fclay-Ca	Fclay-1/Li	Calculated [Li]	δ^7Li_{clays}	Seawater δ^7Li	Seawater δ^7Li	Seawater δ^7Li
			m	wt.%	ppm	‰	‰			of clay ppm	‰	from clays ‰	from carbonate ‰	‰
Yinkeng	34-15	carbonaceous mudstone	12.63	5.84	37.6	1.2	-	0.84	0.83	42.6	1.2	17.2	15-17	17.2
Yinkeng	34-14	carbonaceous mudstone	12.10	6.05	38.4	1.3	-	0.83	0.84	43.6	1.1	17.1	15-17	17.1
Yinkeng	34-13	carbonaceous mudstone	11.58	5.31	38.6	1.2	-	0.85	0.84	43.3	1.1	17.1	15-17	17.1
Yinkeng	34-12	carbonaceous mudstone	11.05	5.18	40.3	1.2	-	0.85	0.86	45.0	1.0	17.0	15-17	17.0
Yinkeng	34-11	claystone	10.52	1.97	25.1	-0.1	-	-	-	-	-	15.9	-	15.9
Yinkeng	34-10	carbonaceous mudstone	10.47	5.78	38.0	1.3	-	0.84	0.84	43.1	1.1	17.1	15-17	17.1
Yinkeng	34-9	carbonaceous mudstone	9.94	5.71	39.1	1.3	-	0.84	0.85	44.1	1.0	17.0	15-17	17.0
Yinkeng	34-8	carbonaceous mudstone	9.41	6.51	34.6	1.0	-	0.82	0.80	39.9	1.4	17.4	15-17	17.4
Yinkeng	34-6	carbonaceous mudstone	8.88	4.61	44.0	1.2	-	0.87	0.89	48.3	0.7	16.7	15-17	16.7
Yinkeng	34-5	carbonaceous mudstone	8.35	6.41	38.2	2.2	-	0.82	0.84	43.5	1.1	17.1	15-17	17.1
Yinkeng	34-4	carbonaceous mudstone	7.86	5.83	34.9	2.0	-	0.84	0.80	39.9	1.5	17.5	15-17	17.5
Yinkeng	34-3	carbonaceous mudstone	7.37	8.23	34.3	2.2	-	0.77	0.80	40.5	1.4	17.4	15-17	17.4
Yinkeng	34-2	carbonaceous mudstone	6.99	4.33	41.2	1.9	-	0.88	0.87	45.4	0.9	16.9	15-17	16.9
Yinkeng	34-1	carbonaceous mudstone	6.49	2.98	49.4	1.4	-	0.92	0.93	52.6	0.4	16.4	15-17	16.4
Yinkeng	33	claystone	6.04	0.95	27.5	-0.3	-	-	-	-	-	15.7	-	15.7
Yinkeng	32-4	carbonaceous mudstone	5.81	5.50	39.5	2.1	-	0.85	0.85	44.4	1.0	17.0	15-17	17.0
Yinkeng	32-3	carbonaceous mudstone	5.67	6.89	36.7	2.1	-	0.81	0.83	42.3	1.2	17.2	15-17	17.2
Yinkeng	32-2	carbonaceous mudstone	5.53	7.44	32.7	2.4	-	0.79	0.78	38.4	1.6	17.6	15-17	17.6
Yinkeng	32-1	carbonaceous mudstone	5.39	10.25	28.7	2.7	-	0.71	0.71	35.5	2.0	18.0	15-17	18.0
Yinkeng	31-2	claystone	5.33	1.51	30.3	-0.3	-	-	-	-	-	15.7	-	15.7
Yinkeng	31-1	claystone	5.25	1.11	25.7	-0.2	-	-	-	-	-	15.8	-	15.8
Yinkeng	30-4	carbonaceous mudstone	5.18	3.09	40.5	2.1	-	0.91	0.86	44.1	1.0	17.0	15-17	17.0
Yinkeng	30-3	carbonaceous mudstone	5.00	13.65	20.4	4.4	-	0.62	0.50	26.9	3.5	19.5	15-17	19.5
Yinkeng	30-2	carbonaceous mudstone	4.82	11.35	24.6	3.7	-	0.68	0.63	31.2	2.6	18.6	15-17	18.6
Yinkeng	30-1	carbonaceous mudstone	4.74	8.32	29.5	2.8	-	0.77	0.73	35.5	2.0	18.0	15-17	18.0
Yinkeng	30-1	carbonaceous mudstone	4.71	14.17	24.8	4.6	-	0.60	0.63	32.7	2.4	18.4	15-17	18.4
Yinkeng	29-1	carbonaceous mudstone	4.42	20.57	18.0	6.8	-	0.42	0.41	26.5	3.6	19.6	15-17	19.6
Yinkeng	27-C(D)	carbonaceous mudstone	4.22	29.14	15.3	9.3	-	0.18	0.27	27.0	3.5	19.5	15-17	19.5

Table S1 continued

Formation	Sample Name	Rock type	Height	CaO	Li	δ^7Li	δ^7Li_{carb}	Fclay-Ca	Fclay-1/Li	Calculated [Li]	δ^7Li_{clays}	Seawater δ^7Li	Seawater δ^7Li	Seawater δ^7Li
			m	wt.%	ppm	‰	‰			of clay ppm	‰	from clays ‰	from carbonate ‰	‰
Yinkeng	26	argillaceous mudstone	4.11	5.13	37.6	0.8	-	0.86	0.83	42.3	1.2	16.8	15-17	16.8
Yinkeng	25-26-3A	claystone	4.09	1.10	30.2	-0.2	-	-	-	-	-	-	15.8	15.8
Yinkeng	25-26-1A	claystone	4.08	1.51	29.0	1.0	-	-	-	-	-	-	17.0	17.0
Yinkeng	25-2A	claystone	4.07	0.91	39.2	0.3	-	-	-	-	-	-	16.3	16.3
Changhsing	24E3-25	chert limestone	4.00	17.54	17.6	12.4	-	-	-	-	-	-	16.0	16.0
Changhsing	24-E1	chert limestone	3.97	48.11	2.1	6.9	-	-	-	-	-	-	10.9	10.9
Changhsing	24-D6	chert limestone	3.73	48.69	1.6	9.0	1.9	-	-	-	-	-	13.0	13.0
Changhsing	24D2-B	chert limestone	3.57	47.96	4.1	7.8	2.6	-	-	-	-	-	11.8	11.8
Changhsing	24-B	chert limestone	3.31	44.43	2.1	12.4	11.0	-	-	-	-	-	16.4	16.4
Changhsing	23-9	chert limestone	3.10	46.14	5.9	7.8		-	-	-	-	-	11.8	11.8
Changhsing	23-7-B	chert limestone	2.89	44.33	6.3	8.0	10.0	-	-	-	-	-	12.0	12.0
Changhsing	23-5	chert limestone	2.67	38.01	10.7	6.7		-	-	-	-	-	10.7	10.7
Changhsing	23-4-down	chert limestone	2.48	33.78	14.1	11.2	11.2	-	-	-	-	-	15.2	15.2
Changhsing	23-2-middle	chert limestone	2.23	51.18	2.7	6.8		-	-	-	-	-	10.8	10.8
Changhsing	23-1-up-C	chert limestone	1.98	50.89	1.9	5.9	11.1	-	-	-	-	-	9.9	9.9
Changhsing	23-1-down	chert limestone	1.92	49.35	3.6	6.9	11.4	-	-	-	-	-	10.9	10.9
Changhsing	22-16	chert limestone	1.81	51.62	1.6	6.6		-	-	-	-	-	10.6	10.6
Changhsing	22-14	chert limestone	1.55	41.92	8.7	6.3	8.3	-	-	-	-	-	10.3	10.3
Changhsing	22-12-13-C	chert limestone	1.46	51.48	1.1	11.2		-	-	-	-	-	15.2	15.2
Changhsing	22-11	chert limestone	0.62	49.83	4.7	8.5	12.0	-	-	-	-	-	12.5	12.5
Changhsing	22-1-B	chert limestone	0.00	33.85	6.2	16.8	14.9	-	-	-	-	-	20.8	20.8

F_{clay}-Ca represent calculated fraction of clays in the studied argillaceous mudstone using diagram of CaO-δ^7Li, where F_{clay}-Ca=1-[CaO]/35.5.

F_{clay}-Li represent calculated fraction of clays in the studied argillaceous mudstone using diagram of 1/[Li]-δ^7Li, where F_{clay}-Li= (1/12-1/$[Li]_{sample}$)/(1/12-1/65)

Calculated [Li] of clays are based on the equation of $[Li]_{clay\ endmember}$=($[Li]_{sample}$-12)/F_{clay}+12

δ^7Li_{clays} is calculated Li isotopic compositions of clay endmember for each sample using 1/[Li]-δ^7Li diagram., δ^7Li_{clays}=171.5/$[Li]_{clay\ endmember}$-2.8475

Seawater δ^7Li calculated from clays using $\Delta^7Li_{SW\text{-}clays}$~ +16‰ and the calculated Li isotopic compositions of clay endmember for each sample.

Seawater δ^7Li calculated from carbonate using $\Delta^7Li_{SW\text{-}carb}$~ +3-5‰ and the calculated Li isotopic compositions of carbonate endmember of ~11.5‰ for samples from Beds 26-34 and the measured Li isotopic compositions of limestones for samples from Beds 22-24

Table S2. Major and trace element concentrations in samples from the Meishan section

Sample Name	Al_2O_3	Fe_2O_3	CaO	MgO	Na_2O	K_2O	TiO_2	MnO	P_2O_5	Li	B	Sc	V	Cr	Co	Ni	Cu	Zn	Ga	Rb	Sr
	wt.%									*trace element in ppm*											
30-4	13.16	7.14	3.09	2.65	0.16	4.81	0.53	0.03	0.35	40.5	57.9	12.4	111	60.3	12.5	32.1	33.7	15.6	19.9	125	144
30-1	7.74	6.00	14.17	7.26	0.09	2.74	0.34	0.08	0.18	24.8	18.9	7.66	50.5	33.7	6.80	17.2	18.1	14.4	10.7	74.6	206
29-1	5.02	5.11	20.57	8.73	0.07	1.72	0.21	0.09	0.15	18.0	19.7	5.80	29.9	20.8	5.55	12.9	15.5	11.6	7.11	47.4	252
27-C(D)	3.30	2.98	29.14	5.18	0.06	1.10	0.15	0.07	0.11	15.3	17.1	4.01	21.3	15.6	2.98	10.5	7.02	10.7	5.14	32.7	239
26	12.10	7.02	5.13	2.54	0.15	4.40	0.49	0.02	0.22	37.6	50.4	12.7	147	68.9	17.2	53.9	34.5	18.1	19.9	133	172
25-26-3A	18.18	4.98	1.10	2.93	0.05	5.97	0.31	0.00	0.25	30.2	168	14.3	39.4	14.2	3.58	15.9	16.0	11.9	25.9	115	112
25-26-1A	18.54	5.86	1.51	2.71	0.06	5.58	0.35	0.01	0.23	29.0	170	15.0	50.8	21.4	4.68	21.7	20.4	16.3	26.0	115	119
25-2A	20.13	3.39	0.91	2.96	0.04	5.41	0.33	0.01	0.21	39.2	177	14.8	11.8	1.79	1.50	4.49	8.06	13.6	29.2	130	143
24e3-25	3.20	19.08	17.54	0.69	0.04	0.86	0.12	0.05	0.15	17.6	6.91	2.88	16.5	19.7	2.59	16.2	22.1	19.3	4.96	19.6	213
24 (e1)	0.27	0.76	48.11	0.90	0.02	0.08	0.01	0.04	0.10	2.10	5.58	0.42	6.15	4.74	0.58	10.7	2.82	18.1	0.58	2.15	545
24-D6	0.14	0.46	48.69	0.69	0.02	0.04	0.01	0.02	0.38	1.56	4.26	0.26	5.36	2.66	0.50	9.73	1.62	13.5	0.29	1.25	1151
24D2-B	0.45	0.69	47.96	1.04	0.02	0.15	0.02	0.01	0.07	4.10	5.43	0.57	11.3	7.13	0.85	12.6	3.29	13.4	0.74	4.93	544
24-B	0.19	0.57	44.43	0.81	0.02	0.06	0.01	0.01	0.09	2.10	4.77	0.34	8.62	5.92	0.42	10.2	2.77	10.3	0.29	1.79	788
23-9	0.79	0.94	46.14	1.18	0.03	0.26	0.03	0.01	0.22	5.94	7.95	1.11	21.3	12.9	1.39	16.1	8.03	10.4	1.29	9.16	769
23-7-B	0.87	1.03	44.33	0.87	0.03	0.30	0.04	0.01	0.28	6.35	10.7	1.22	15.7	17.1	1.45	17.0	8.62	10.1	1.41	10.3	612
23-5	1.73	1.18	38.01	0.91	0.04	0.55	0.03	0.01	0.39	10.7	9.48	1.90	49.3	34.6	1.80	26.1	22.0	12.9	2.58	17.9	632
23-4-down	1.55	1.04	33.78	0.58	0.05	0.45	0.01	0.01	1.16	14.1	14.3	2.17	17.9	26.6	0.78	17.3	19.6	11.7	2.43	12.8	507
23-2-middle	0.22	0.55	51.18	1.18	0.03	0.08	0.01	0.01	0.49	2.68	5.23	0.49	10.8	4.82	0.64	11.3	3.89	10.6	0.45	2.73	793
23-1-up-C	0.21	0.49	50.89	1.08	0.03	0.07	0.01	0.01	0.44	1.90	4.84	0.35	6.87	4.17	0.62	10.7	2.92	10.1	0.39	2.38	931
23-1-down	0.56	0.68	49.35	1.02	0.03	0.16	0.01	0.01	0.68	3.65	7.00	1.01	10.2	6.51	1.87	12.9	5.49	10.2	0.70	5.15	754
22-16	0.13	0.45	51.62	1.04	0.03	0.04	0.00	0.01	0.85	1.64	4.84	0.42	4.27	3.64	0.52	10.6	2.85	9.11	0.23	1.23	811
22-14	1.52	0.92	41.92	0.94	0.06	0.46	0.00	0.01	3.45	8.70	19.5	1.65	23.3	20.9	1.85	18.1	19.9	10.4	1.98	13.6	742
22-12-13-C	0.09	0.44	51.48	0.79	0.03	0.03	0.01	0.01	1.12	1.09	4.88	0.22	6.76	1.96	0.50	10.2	1.44	10.3	0.18	0.96	876
22-11	0.52	0.66	49.83	0.77	0.03	0.16	0.02	0.01	0.14	4.65	6.10	0.56	7.13	3.86	0.60	9.65	4.07	7.16	0.74	5.73	1040
22-1-B	0.68	0.73	33.85	0.61	0.04	0.18	0.03	0.01	0.22	6.19	9.47	0.77	10.0	6.68	1.05	10.7	4.83	10.6	1.20	7.48	469

Table S2 continued

Sample Name	Y	Zr	Nb	Ba	La	Ce	Pr	Nd	Sm	Eu	Gd	Tb	Dy	Ho	Er	Tm	Yb	Lu	Hf	Pb	Th	U
	trace element in ppm																					
30-4	22.5	120	20.9	272	38.5	73.1	8.50	30.3	5.80	0.90	5.33	0.86	4.63	0.96	2.78	0.44	2.90	0.45	3.76	27.4	12.9	7.28
30-1	19.1	78.1	9.85	158	26.5	50.3	6.28	22.7	4.43	0.83	4.32	0.68	3.53	0.72	1.93	0.28	1.74	0.26	2.37	11.1	8.96	2.15
29-1	21.9	51.3	6.29	97.4	24.1	42.4	5.79	21.5	4.31	0.82	4.36	0.68	3.50	0.72	1.92	0.27	1.67	0.26	1.49	9.69	5.66	1.52
27-C(D)	29.9	35.8	4.55	135	27.9	43.1	6.16	23.3	4.73	0.89	5.08	0.80	4.29	0.92	2.58	0.36	2.19	0.33	1.09	7.54	4.12	1.76
26	20.0	115	15.1	254	39.4	67.8	8.12	29.2	5.44	0.90	5.04	0.77	4.07	0.83	2.37	0.37	2.44	0.37	3.56	43.8	15.5	6.86
25-26-3A	32.7	286	18.7	44.3	43.0	99.5	11.9	43.5	8.28	0.98	7.66	1.31	7.34	1.50	4.10	0.59	3.55	0.51	10.7	47.4	47.0	7.35
25-26-1A	32.2	274	19.1	66.2	48.4	110	13.1	47.5	8.81	1.05	7.92	1.30	7.12	1.44	3.91	0.56	3.40	0.49	9.81	56.6	42.9	7.68
25-2A	38.1	340	24.0	20.6	47.2	111	13.3	47.8	9.32	1.08	8.64	1.51	8.44	1.68	4.48	0.62	3.60	0.51	12.1	41.6	53.5	7.50
24e3-25	23.9	42.0	12.4	76.5	24.4	47.6	6.48	24.9	5.64	0.83	5.76	0.95	5.08	1.04	2.92	0.44	3.05	0.47	1.33	57.5	5.75	9.37
24 (e1)	21.0	3.96	0.45	66.8	12.9	17.7	2.17	8.39	1.87	0.26	2.48	0.44	2.76	0.66	2.02	0.30	1.87	0.29	0.12	5.14	0.49	5.16
24-D6	2.55	2.23	0.20	68.3	2.01	3.20	0.40	1.50	0.30	0.06	0.34	0.06	0.32	0.07	0.21	0.03	0.19	0.03	0.05	1.89	0.29	3.57
24D2-B	3.39	6.59	0.70	10.6	2.40	4.02	0.50	1.84	0.39	0.07	0.43	0.07	0.42	0.09	0.28	0.04	0.26	0.04	0.16	4.70	0.65	2.46
24-B	3.15	2.55	0.23	10.6	2.66	4.44	0.56	2.06	0.41	0.07	0.44	0.07	0.40	0.09	0.26	0.04	0.23	0.04	0.06	2.31	0.33	1.64
23-9	6.36	8.46	0.98	37.6	6.62	10.6	1.43	5.34	1.05	0.20	1.09	0.17	0.89	0.19	0.52	0.07	0.44	0.07	0.24	3.79	1.18	4.68
23-7-B	5.59	9.08	1.13	18.1	5.60	10.3	1.27	4.77	0.96	0.18	0.99	0.15	0.83	0.17	0.48	0.07	0.43	0.06	0.25	4.45	1.51	3.16
23-5	7.16	18.4	1.11	34.6	6.10	9.86	1.41	5.32	1.15	0.23	1.20	0.19	1.05	0.22	0.63	0.09	0.59	0.09	0.45	5.76	2.41	5.73
23-4-down	14.4	17.7	0.57	22.5	10.2	16.2	2.46	9.42	2.20	0.38	2.46	0.42	2.40	0.49	1.38	0.19	1.21	0.18	0.38	6.46	2.95	4.31
23-2-middle	4.09	3.98	0.35	4.78	3.35	4.81	0.67	2.56	0.55	0.11	0.62	0.10	0.56	0.12	0.34	0.05	0.29	0.04	0.11	0.74	0.58	3.02
23-1-up-C	2.01	2.70	0.31	4.49	1.71	2.72	0.36	1.34	0.28	0.06	0.31	0.05	0.27	0.06	0.16	0.02	0.14	0.02	0.07	0.52	0.42	2.02
23-1-down	6.15	5.36	0.49	6.55	5.55	8.10	1.04	3.77	0.78	0.15	0.87	0.14	0.81	0.17	0.51	0.08	0.51	0.08	0.16	1.68	1.01	3.82
22-16	3.90	1.69	0.18	3.16	2.45	3.23	0.49	1.94	0.44	0.10	0.53	0.09	0.50	0.11	0.30	0.04	0.26	0.04	0.04	0.41	0.34	3.15
22-14	14.8	19.9	0.22	23.6	10.4	15.4	2.51	10.0	2.30	0.43	2.56	0.42	2.31	0.47	1.28	0.17	1.10	0.17	0.54	4.79	3.42	10.8
22-12-13-C	2.02	1.56	0.15	2.45	1.68	2.82	0.34	1.30	0.28	0.05	0.32	0.05	0.28	0.06	0.16	0.02	0.13	0.02	0.04	0.44	0.31	3.00
22-11	2.42	6.08	0.78	8.37	3.30	5.84	0.69	2.46	0.46	0.08	0.46	0.07	0.36	0.07	0.21	0.03	0.20	0.03	0.17	1.32	1.17	1.43
22-1-B	5.65	7.88	1.60	15.5	4.19	7.46	0.83	3.07	0.65	0.11	0.73	0.12	0.73	0.16	0.47	0.07	0.42	0.06	0.19	2.42	0.96	2.99

Table S3 Input parameters for seawater Li isotope modeling

Run parameters	Total Li_{SW} 10^{10}mole	F_{Riv} 10^{10}mole/yr	δ^7Li_{Riv} ‰	F_{HT} 10^{10}mole/yr	δ^7Li_{HT} ‰	F_{SR} 10^{10}mole/yr	δ^7Li_{SR} ‰	F_{SC} 10^{10}mole/yr	δ^7Li_{SC} ‰	δ^7Li_{SW} ‰
Start parameters	3.4×10^6	1	23	1.3	8	0.6	15	2.9	15	31
Steady state -1	3.4×10^6	1	2, 5, 10, 20	1.3	8	0.6	15	F_{input}	15	Fig. S11
Steady state -2	3.4×10^6	1, 5, 10, 15	2	1.3	8	0.6	15	F_{input}	15	Fig. S12
Steady state -3	3.4×10^6	1	23	0.5, 1.3, 5, 10, 20	8	0.6	15	F_{input}	15	Fig. S13
Steady state -4	3.4×10^6	5, 10, 15	2	1, 5	8	0.6	15	F_{input}	15	Fig. S14
Dynamic -1	Nt	1	23	0.5, 1.3, 5, 10, 20	8	0.6	15	kNt	15	Fig. S15
Dynamic -2	Nt	5, 10	10, 23	1.3	8	0.6	15	kNt	15	Fig. S16
Dynamic -3	Nt	5, 10, 15, 20	4	1.3	8	0.6	15	kNt	15	Fig. S17
Dynamic	Nt	18, to 1	4, to 23	1.3	8	0.6	15	kNt	15	Fig.2

Start parameters are modern values from ref (9). In the stead state model, F_{SC} always equal to F_{input}, lead to constant seawater Li reservoir ~3.4×10^{16}mole. In the dynamic model, as described in supplementary text, F_{SC} is a function of seawater Li concentration, thus forming a feedback system on seawater Li reservoir and Li input fluxes. Detailed modeling parameters for Fig.2 in the main text are also listed in the table. The F_{riv} was initially set at high levels of ~18 times of present values for 300Kyr, and then changed to 1×10^{10}mole/yr for 400Kyr. The δ^7Li_{riv} was initially set at light values of ~4‰ for 300Kyr, and then changed to 23‰ for another 400Kyr.

IV. Supplemental References

1. Huh Y, Chan LH, Chadwick OA (2004) Behavior of lithium and its isotopes during weathering of Hawaiian basalt. *Geochem Geophy Geosy* 5(9):1-22.
2. Huh Y, Chan L-H, Edmond JM (2001) Lithium isotopes as a probe of weathering processes: Orinoco River. *Earth Planet. Sci. Lett.* 194(1):189-199.
3. Kısakűrek B, James RH, Harris NB (2005) Li and δ^7Li in Himalayan rivers: Proxies for silicate weathering? *Earth Planet. Sci. Lett.* 237(3):387-401.
4. Tomascak PB (2004) Developments in the understanding and application of lithium isotopes in the earth and planetary sciences. *Rev Mineral Geochem* 55(1):153-195.
5. Teng F-Z*, et al.* (2004) Lithium isotopic composition and concentration of the upper continental crust. *Geochim. Cosmochim. Acta* 68(20):4167-4178.
6. Wimpenny J*, et al.* (2010) The behaviour of Li and Mg isotopes during primary phase dissolution and secondary mineral formation in basalt. *Geochim. Cosmochim. Acta* 74(18):5259-5279.
7. Pogge von Strandmann PAE*, et al.* (2006) Riverine behaviour of uranium and lithium isotopes in an actively glaciated basaltic terrain. *Earth Planet. Sci. Lett.* 251(1):134-147.
8. von Strandmann PAE, Burton KW, James RH, van Calsteren P, Gislason SR (2010) Assessing the role of climate on uranium and lithium isotope behaviour in rivers draining a basaltic terrain. *Chem Geol* 270(1):227-239.
9. Misra S, Froelich PN (2012) Lithium isotope history of Cenozoic seawater: Changes in silicate weathering and reverse weathering. *Science* 335(6070):818-823.
10. Liu X-M, Rudnick RL, McDonough WF, Cummings ML (2013) Influence of chemical weathering on the composition of the continental crust: Insights from Li and Nd isotopes in bauxite profiles developed on Columbia River Basalts. *Geochim. Cosmochim. Acta* 115(0):73-91.
11. von Strandmann PAE, Jenkyns HC, Woodfine RG (2013) Lithium isotope evidence for enhanced weathering during Oceanic Anoxic Event 2. *Nat Geosci* 6(8):668-672.
12. Kump LR, Brantley SL, Arthur MA (2000) Chemical weathering, atmospheric CO_2, and climate. *Annu Rev Earth Planet Sci* 28(1):611-667.
13. Hathorne EC, James RH (2006) Temporal record of lithium in seawater: A tracer for silicate weathering? *Earth Planet. Sci. Lett.* 246(3):393-406.
14. Chan LH, Gieskes JM, You CF, Edmond JM (1994) Lithium isotope geochemistry of sediments and hydrothermal fluids of the Guaymas Basin, Gulf of California. *Geochim. Cosmochim. Acta* 58(20):4443-4454.
15. Elderfield H, Schultz A (1996) Mid-ocean ridge hydrothermal fluxes and the chemical composition of the ocean. *Annu Rev Earth Planet Sci* 24:191-224.
16. Chan LH, Edmond JM, Thompson G, Gillis K (1992) Lithium isotopic composition of submarine basalts: implications for the lithium cycle in the oceans. *Earth Planet. Sci. Lett.* 108(1):151-160.
17. Vigier N*, et al.* (2008) Quantifying Li isotope fractionation during smectite formation and implications for the Li cycle. *Geochim. Cosmochim. Acta* 72(3):780-792.
18. Jeffcoate AB, Elliott T, Thomas A, Bouman C (2004) Precise/small sample size determinations of lithium isotopic compositions of geological reference materials and modern seawater by MC‐ICP‐MS. *Geostand Geoanal Res* 28(1):161-172.
19. Marriott CS, Henderson GM, Belshaw NS, Tudhope AW (2004) Temperature dependence of δ^7Li, δ^{44}Ca and Li/Ca during growth of calcium carbonate. *Earth Planet. Sci. Lett.* 222(2):615-624.
20. Marriott CS, Henderson GM, Crompton R, Staubwasser M, Shaw S (2004) Effect of mineralogy, salinity, and temperature on Li/Ca and Li isotope composition of calcium carbonate. *Chem Geol* 212(1):5-15.
21. Chan LH, Leeman WP, Plank T (2006) Lithium isotopic composition of marine sediments. *Geochem Geophy Geosy* 7(6):1-25.
22. Chan L-H, Alt JC, Teagle DA (2002) Lithium and lithium isotope profiles through the upper oceanic crust: a study of seawater–basalt exchange at ODP Sites 504B and 896A. *Earth Planet. Sci. Lett.* 201(1):187-201.
23. Pourmand A, Dauphas N, Ireland TJ (2012) A novel extraction chromatography and MC-ICP-MS technique for rapid analysis of REE, Sc and Y: Revising CI-chondrite and Post-Archean Australian Shale (PAAS) abundances. *Chem Geol* 291:38-54.
24. Azmy K*, et al.* (2011) Biogenic and abiogenic low-Mg calcite (bLMC and aLMC): Evaluation of

seawater-REE composition, water masses and carbonate diagenesis. *Chem Geol* 280(1):180-190.
25. Yin H, Xie S, Luo G, Algeo TJ, Zhang K (2012) Two episodes of environmental change at the Permian–Triassic boundary of the GSSP section Meishan. *Earth-Sci. Rev.* 115(3):163-172.
26. Michalopoulos P, Aller RC (1995) Rapid clay mineral formation in Amazon delta sediments: reverse weathering and oceanic elemental cycles. *Science*:614-614.
27. Plank T, Langmuir CH (1998) The chemical composition of subducting sediment and its consequences for the crust and mantle. *Chem Geol* 145(3):325-394.
28. Gao S*, et al.* (1998) Chemical composition of the continental crust as revealed by studies in East China. *Geochim. Cosmochim. Acta* 62(11):1959-1975.
29. Zhang J, Liang H, He X, Yang Y, Chen B (2011) Sulfur isotopes of framboidal pyrite in the Permian-Triassic boundary clay at Meishan section. *Acta Geologica Sinica - English Edition* 85(3):694-701.
30. Montes CR, Melfi AJ, Carvalho A, Vieira-Coelho AC, Formoso ML (2002) Genesis, mineralogy and geochemistry of kaolin deposits of the Jari River, Amapá State, Brazil. *Clays Clay Miner* 50(4):494-503.
31. Fernandez R, Martirena F, Scrivener KL (2011) The origin of the pozzolanic activity of calcined clay minerals: a comparison between kaolinite, illite and montmorillonite. *Cement Concrete Res* 41(1):113-122.
32. Mermut AR, Cano AF (2001) Baseline studies of the clay minerals society source clays: chemical analyses of major elements. *Clays Clay Miner* 49(5):381-386.
33. Elliott T, Plank T, Zindler A, White W, Bourdon B (1997) Element transport from slab to volcanic front at the Mariana arc. *J. Geophys. Res.* 102(B7):14991-15019.
34. Maxwell JA (1963) *Geochemical study of some chert and related deposits* (Department of Mines and Technical Surveys, Canada).
35. Hoefs J, Sywall M (1997) Lithium isotope composition of Quaternary and Tertiary biogene carbonates and a global lithium isotope balance. *Geochim. Cosmochim. Acta* 61(13):2679-2690.
36. Gieskes JM (1981) Deep-sea drilling interstitial water studies: implications for chemical alteration of the oceanic crust, layers I and II. *The Deep Sea Drilling Project: A Decade of Progress. Spec. Publ.—Soc. Econ. Paleontol. Mineral* 32:149-167.
37. Mirota MD, Veizer J (1994) Geochemistry of precambrian carbonates: VI. Aphebian albanel formations, Quebec, Canada. *Geochim. Cosmochim. Acta* 58(7):1735-1745.
38. Misra S, Froelich PN (2009) Measurement of lithium isotope ratios by quadrupole-ICP-MS: application to seawater and natural carbonates. *J Anal Atom Spectrom* 24(11):1524-1533.
39. Scholz F*, et al.* (2010) Lithium isotope geochemistry of marine pore waters–insights from cold seep fluids. *Geochim. Cosmochim. Acta* 74(12):3459-3475.
40. Chan L-H, Kastner M (2000) Lithium isotopic compositions of pore fluids and sediments in the Costa Rica subduction zone: implications for fluid processes and sediment contribution to the arc volcanoes. *Earth Planet. Sci. Lett.* 183(1):275-290.
41. You C-F, Chan L, Spivack A, Gieskes J (1995) Lithium, boron, and their isotopes in sediments and pore waters of Ocean Drilling Program Site 808, Nankai Trough: Implications for fluid expulsion in accretionary prisms. *Geology* 23(1):37-40.
42. Williams LB, Hervig RL (2005) Lithium and boron isotopes in illite-smectite: the importance of crystal size. *Geochim. Cosmochim. Acta* 69(24):5705-5716.
43. Chan LH, Edmond JM, Thompson G (1993) A lithium isotope study of hot springs and metabasalts from mid‐ocean ridge hydrothermal systems. *J Geophy Res: Solid Earth* 98(B6):9653-9659.
44. Huh Y, Chan L-H, Zhang L, Edmond JM (1998) Lithium and its isotopes in major world rivers: implications for weathering and the oceanic budget. *Geochim. Cosmochim. Acta* 62(12):2039-2051.
45. Seyfried Jr W, Chen X, Chan L-H (1998) Trace element mobility and lithium isotope exchange during hydrothermal alteration of seafloor weathered basalt: an experimental study at 350 C, 500 bars. *Geochim. Cosmochim. Acta* 62(6):949-960.
46. Jeffcoate A*, et al.* (2007) Li isotope fractionation in peridotites and mafic melts. *Geochim. Cosmochim. Acta* 71(1):202-218.
47. Yin H*, et al.* (2014) The end-Permian regression in South China and its implication on mass extinction. *Earth-Sci. Rev.* 137:19–33.

48. Veevers J (2004) Gondwanaland from 650–500 Ma assembly through 320 Ma merger in Pangea to 185–100 Ma breakup: supercontinental tectonics via stratigraphy and radiometric dating. *Earth-Sci. Rev.* 68(1):1-132.
49. Erwin DH, Bowring SA, Yugan J (2002) End-Permian mass extinctions: a review. *Geol Soc Am*:363-384.
50. Korte C, Jasper T, Kozur HW, Veizer J (2006) $^{87}Sr/^{86}Sr$ record of Permian seawater. *Palaeogeogr Palaeoclimatol Palaeoecol* 240(1):89-107.
51. Martin EE, Macdougall JD (1995) Sr and Nd isotopes at the Prmian/Triassic boundary: A record of climate change. *Chem Geol* 125(1–2):73-99.
52. Prokoph A, Shields GA, Veizer J (2008) Compilation and time-series analysis of a marine carbonate δ 18 O, δ 13 C, 87 Sr/ 86 Sr and δ 34 S database through Earth history. *Earth-Sci. Rev.* 87(3):113-133.
53. Song H*, et al.* (2015) Integrated Sr isotope variations and global environmental changes through the Late Permian to early Late Triassic. *Earth Plane Sci. Lett.* 424:140-147.
54. Burgess SD, Bowring SA (2015) High-precision geochronology confirms voluminous magmatism before, during, and after Earth's most severe extinction. *Sci Adv* 1(7):e1500470-e1500470.
55. Svensen H*, et al.* (2009) Siberian gas venting and the end-Permian environmental crisis. *Earth Planet. Sci. Lett.* 277(3):490-500.
56. Reichow MK*, et al.* (2009) The timing and extent of the eruption of the Siberian Traps large igneous province: Implications for the end-Permian environmental crisis. *Earth Planet. Sci. Lett.* 277(1):9-20.
57. Renne PR, Black MT, Zichao Z, Richards MA, Basu AR (1995) Synchrony and Causal Relations Between Permian-Triassic Boundary Crises and Siberian Flood Volcanism. *Science* 269(5229):1413-1416.
58. Schneebeli-Hermann E*, et al.* (2013) Evidence for atmospheric carbon injection during the end-Permian extinction. *Geology* 41(5):579-582.
59. Joachimski MM*, et al.* (2012) Climate warming in the latest Permian and the Permian-Triassic mass extinction. *Geology* 40(3):195-198.
60. Maruoka T, Koeberl C, Hancox P, Reimold W (2003) Sulfur geochemistry across a terrestrial Permian–Triassic boundary section in the Karoo Basin, South Africa. *Earth Planet. Sci. Lett.* 206(1):101-117.
61. Depetris PJ, Pasquini AI, Lecomte KL (2014) *Weathering and the Riverine Denudation of Continents* (Springer Netherlands).